Mode change of millennial CO_2 variability during the last glacial cycle associated with a bipolar marine carbon seesaw

Bernhard Bereiter[a,b,1], Dieter Lüthi[a,b], Michael Siegrist[a,b], Simon Schüpbach[a,b], Thomas F. Stocker[a,b], and Hubertus Fischer[a,b]

[a]Climate and Environmental Physics, Physics Institute, University of Bern, Sidlerstrasse 5, CH-3012 Bern, Switzerland; and [b]Oeschger Center for Climate Change Research, University of Bern, Zaehringerstrasse 25, CH-3012 Bern, Switzerland

Important elements of natural climate variations during the last ice age are abrupt temperature increases over Greenland and related warming and cooling periods over Antarctica. Records from Antarctic ice cores have shown that the global carbon cycle also plays a role in these changes. The available data shows that atmospheric CO_2 follows closely temperatures reconstructed from Antarctic ice cores during these variations. Here, we present new high-resolution CO_2 data from Antarctic ice cores, which cover the period between 115,000 and 38,000 y before present. Our measurements show that also smaller Antarctic warming events have an imprint in CO_2 concentrations. Moreover, they indicate that during Marine Isotope Stage (MIS) 5, the peak of millennial CO_2 variations lags the onset of Dansgaard/Oeschger warmings by 250 ± 190 y. During MIS 3, this lag increases significantly to 870 ± 90 y. Considerations of the ocean circulation suggest that the millennial variability associated with the Atlantic Meridional Overturning Circulation (AMOC) undergoes a mode change from MIS 5 to MIS 4 and 3. Ocean carbon inventory estimates imply that during MIS 3 additional carbon is derived from an extended mass of carbon-enriched Antarctic Bottom Water. The absence of such a carbon-enriched water mass in the North Atlantic during MIS 5 can explain the smaller amount of carbon released to the atmosphere after the Antarctic temperature maximum and, hence, the shorter lag. Our new data provides further constraints for transient coupled carbon cycle-climate simulations during the entire last glacial cycle.

abrupt climate change | CO_2-temperature phasing | ice age variability | paleoclimate | greenhouse gas

The climate of the last glacial period is characterized by low global mean temperatures and a number of interhemispheric variations on time scales of several millennia. In the northern hemisphere, in particular on the Greenland ice sheet, large and very rapid temperature jumps of up to 15 °C within a few decades, followed by more steady decreases of temperature, have been identified from ice core analyses (1, 2). 25 of these so-called Dansgaard-Oeschger (DO) events have been found during the last glacial period. For each of these events, an associated Antarctic temperature variation has been also documented in Antarctic ice cores (Antarctic Isotope Maximum [AIM] events) (3). Antarctic temperatures increase steadily when Greenland is in the cold phase and slowly decrease following the abrupt temperature increase in Greenland during a DO event. This behavior is explained by the concept of an oceanic thermal bipolar seesaw, where variations in the Atlantic Meridional Overturning Circulation (AMOC) and associated changes in heat transport across the equator to the North Atlantic modulate the southern and northern hemisphere temperatures during each of these events (4).

Previous reconstructions of atmospheric CO_2 concentrations during these millennial-scale variations show that CO_2 varies largely in parallel with the major AIM events (5, 6). Those data indicate stable CO_2 concentrations for up to 2,000 y after the peak of major AIM events during marine isotope stage (MIS)

3; however, data coverage and resolution are not sufficient to completely resolve CO_2 during the seesaw variability of the entire MIS 5–2 time period.

Here we present a new CO_2 record from the Talos Dome ice core (TALDICE, 159 °E; 73 °S) with 116 data points and an average resolution of 280 y and an extended record from the EPICA (European Project for Ice Coring in Antarctica) ice core retrieved in Dronning Maud Land (EDML, 0 °E; 75 °S) (7) with 92 new data points and 450 y average resolution going back to 115,000 y before present (115 kyr BP, where present refers to 1950). Together, the records permit a detailed insight into the coupled carbon cycle-climate dynamics over the time period from 115 to 38 kyr BP. For most parts of the TALDICE core, atmospheric CH_4 concentration data are available with a resolution of a few decades (8). The resolution of the available EDML CH_4 record (3, 9–11) is 170 y on average. The dense data coverage of CH_4 and CO_2 in both cores, the fact that all DO event onsets are associated with a rapid increase of atmospheric CH_4 concentrations (10), and the low CO_2 measurement uncertainty of better than 1.5 ppm by volume (ppmv) (*Materials and Methods*) allow us to investigate the interplay of variations in the bipolar seesaw and CO_2 in unprecedented detail. This new analysis offers new insights into mechanisms responsible for millennial carbon cycle variations during the last ice age and also provides further constraints for transient simulations using coupled carbon cycle-climate models.

Results

In Fig. 1, the TALDICE and EDML CO_2 records are shown, as well as the previously published records of the Byrd (6), Taylor Dome (5), and Vostok (12) ice cores. With the exception of the Vostok record, all records are synchronized on the EDML1 Scenario 4 gas age scale (13) by matching tie points in the CH_4 records (*SI Text*). There is a clear correlation of the CO_2 records where they overlap. However, the different cores show offsets of a few ppmv during certain parts of the records. These offsets are discussed in detail in the *SI Text*. Note that the offsets only affect the overall concentration level in the individual cores but not the temporal CO_2 changes; thus, also not the phase relationship between CO_2 and the onset of DO events investigated in this study. Accordingly, they do not affect the conclusions drawn in our study. Our two new records represent the temporal evolution of CO_2 in even more detail than previous records, because the main features are covered by two independent ice cores, the
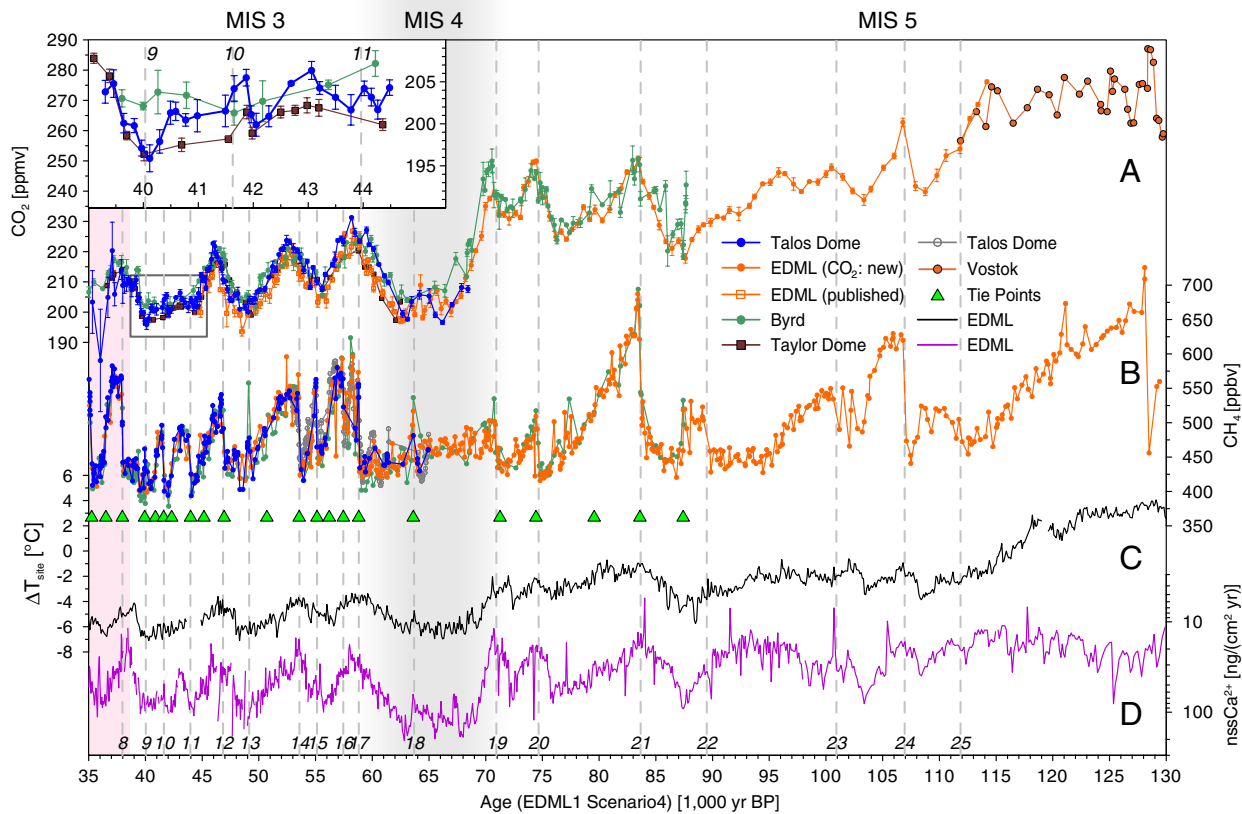
Fig. 1. Compilation of atmospheric and proxy records measured on different ice cores from 130 to 35 kyr BP. (*A*) atmospheric CO_2 concentrations from different ice cores [blue: Talos Dome ice core (TALDICE) (this study); orange dots: EDML (this study) (115 to 64 kyr BP)]; orange squares: EDML (7); dark brown: Taylor Dome (5); green: Byrd (6); red brown: Vostok (12). (*B*) CH_4 concentrations (3, 10, 11) [same color code as above, including continuous flow analysis data from TALDICE (gray) (8)]. Green triangles show the tie points for age scale synchronization. (*C*) ΔT record (reference temperature is the average from 1.2–2 kyr BP) from the EDML ice core (40). (*D*) non-sea salt (nss) Ca^{2+} flux measured at the EDML ice core (19). With the exception of the Vostok data, all records are synchronized to and plotted on the EDML1 Scenario 4 age scale (13). Dashed lines indicate the jump in CH_4 associated with DO events. The numbers of the DO, AIM events, and CDM, respectively, are given in italics at the bottom (*Inset Top*) of the dashed lines. The gray-shaded area indicates MIS 4. The pink area marks the region subject to strong fractionation of the TALDICE CO_2 record in the bubble-clathrate transformation zone (7). The inset shows an enlargement of the CO_2 data during DO 9–11, as indicated by the gray rectangle.

ice storage time is more than 10 times shorter than that of the Byrd core reducing potential storage-related gas fractionation and diffusion effects in the ice (14), and because of the high temporal resolution of the data.

During MIS 3, the new features seen in the TALDICE and EDML CO_2 records are: (*i*) both cores demonstrate that carbon dioxide maxima (CDM) associated with the major AIM events of MIS 3 (AIM events 12, 14, 17) have a clear peak rather than a phase of stable CO_2 concentrations as previously reported (Fig. 2) (6); (*ii*) these peaks of CDM 12, 14, and 17 lag the onset of the corresponding DO event by nearly 1 kyr (Fig. 2); (*iii*) CO_2 varies also during phases of smaller AIM events (9–11) (Fig. 1, *Inset*). Compared to the CDM associated with the major AIM events, these CDM show a four to five times smaller amplitude (5 ppmv) and no significant phase relationship with the DO events and AIM events, respectively.

During the slow glaciation in the course of MIS 5, five CDM can be identified with a clear corresponding DO event (15–19), with CDM 23 and 24 (numbered according to their corresponding DO event) being resolved here for the first time. For CDM 20, 21, and 23, our record shows a steady increase before the peak of the CDM, as was the case during MIS 3 CDM, instead of a CO_2 jump as reported (6). Compared to MIS 3, CDM during MIS 5 show a significantly shorter lag relative to the DO onset (Fig. 2). The CDM counterparts of DO 22 and 25 are missing, probably due to the smaller temperature amplitude of these two events. Note that between DO 22 and 23, a CDM is found that cannot

be attributed to a DO event documented in CH_4 and Greenland temperature records.

To quantify the different lags between the CO_2 peaks and the onset of DO events, the following analysis has been performed: First, for all CDM, a time marker of the corresponding DO event onset was identified using CH_4 records (*SI Text*), thus avoiding any error in the ice age/gas age difference. Second, through all CO_2 data points within 3,000 y before and after this marker (Fig. 2) splines with a cut-off period of 500 y and with data points varied within a Gaussian distribution with a width defined by the measurement uncertainty have been calculated (Monte Carlo splines) (*SI Text*). From these splines, an average lag and CO_2 increase after the DO onset, as well as the corresponding standard deviations, have been calculated for each CDM (Fig. 2, *Insets*). The uncertainty of each DO onset time marker was added to the lag uncertainties. For MIS 3, this analysis shows a lag of the CO_2 peak of 670 ± 360 y (one sigma) for EDML records and 870 ± 90 y for TALDICE records, respectively, where the estimate of the TALDICE record is assumed to be more accurate, due to the narrower age distribution of the occluded air in this ice core. During MIS 5, the lag is only 260 ± 220 y using all MIS 5 events found in the EDML record. The EDML records during CDM 23 and 24 suffer from some weaknesses: The DO trigger (*SI Text*), as well as the large delay uncertainty of CDM 23, casts doubt on the corresponding results; the resolution of CDM 24 is rather coarse for the splines applied here (*SI Text*). Therefore, data from the EPICA Dome Concordia (EDC) ice core for CDM 24 (20) were added (Fig. 2) as they are slightly better
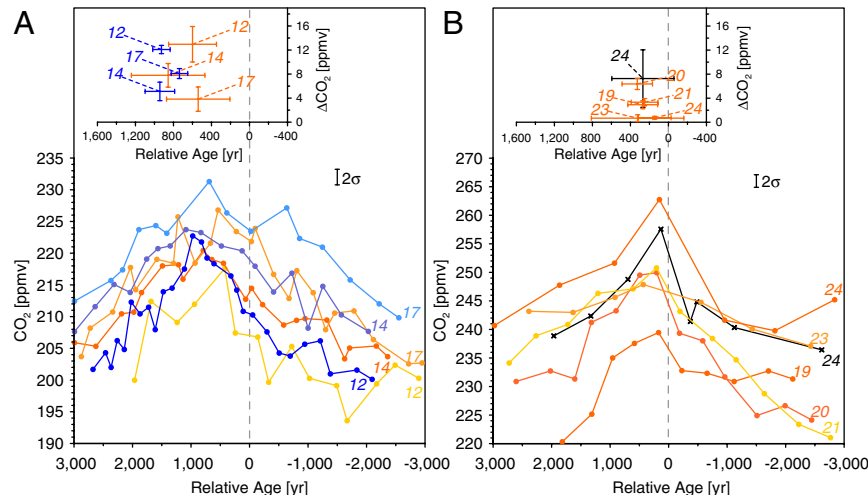
Fig. 2. Shift of CDM relative to DO onset. (*A*) CO_2 data during MIS 3. Time zero corresponds to the onset of the DO event and the corresponding CH_4 jump, respectively (*SI Text*). We assume that the increase in CH_4 was always synchronous to the rapid temperature increase within ± 50 y (2) as documented in Greenland throughout the last glacial cycle. *Inset*: Calculated delay of CDM relative to the DO onset (*x* axis) and increase of CO_2 after the DO onset (*y* axis) for every CDM plotted, using a Monte Carlo spline routine (*SI Text*). (*B*) As left but with data during MIS 5. Bluish colors indicated data from the TALDICE, orange colors data from the EDML, and black colors data from the EDC ice core (20). The 2σ error bars indicate the average uncertainty of all shown data points.

resolved around CDM 24. The results from CDM 23 were excluded. With this approach, the delay estimate for MIS 5 is 250 ± 190 y. Both estimates show almost the same probability of about 90% that delays during MIS 5 are larger than zero.

The significance of the different lags between MIS 3 and 5 was tested using two different statistical tests: an independent two-sample *t*-test and a Wilcoxon rank-sum test (or Mann-Whitney *U* test) (*SI Text*). With respect to the conservative strategy applied for the tests, the significance that the lags in MIS 3 and 5 are different is around 95%, when only EDML data are used. As mentioned above, however, the EDML records have some weaknesses at CDM 23 and 24. By excluding CDM 23 and complementing CDM 24 with data from the EDC ice core, significance can be slightly increased. Also, the estimates of the TALDICE record can be used as independent measures of events during MIS 3. When these estimates are included, the significance exceeds 97.5%. In summary, we conclude that the peak in the CDM during MIS 3 relative to the onset of DO events occurs significantly later than in MIS 5. If we assume a perfect bipolar seesaw relationship between the North Atlantic and the Southern Ocean realm, that would also imply a lag of CDM relative to the respective maximum warming in Antarctica.

Further features of the CDM, such as their amplitudes, duration, and CO_2 rates of change, have been investigated. A systematic and objective estimate of the amplitudes and the duration is difficult in particular for the MIS 5 period, since the CO_2 concentration baseline during the events cannot be defined precisely enough. The amplitudes and duration of the MIS 3 CDM are 20–30 ppmv and 4,500–6,500 y, respectively, as already found in earlier studies (5, 6). Regarding the CO_2 rates of change, we used splines with a cut-off period of 1,000 y and calculated the rates before the peak of the CDM (*SI Text*). For the MIS 3 events, these rates are 6.1 ± 0.6 ppmv/kyr which is–with the exception of CDM 23–two to four times slower than for the individual MIS 5 events. Note, however, that the time windows which are used to calculate these rates for the MIS 5 events contain in some cases only two data points. When all MIS 5 events are included, the rate of change for the MIS 3 events is two times smaller on average. In summary, CO_2 increases of the CDM tend to be faster during MIS 5 compared to MIS 3; however, future CO_2 measurements in higher temporal resolution will be needed to validate this result.

A further clear difference between MIS 5 and 3 events is the CO_2 concentration baseline, i.e., its long-term average for both time periods. The change of this baseline occurs at the MIS 5–4 transition (6, 12). With our new records, we can determine this CO_2 drop to be 28 ppmv within 2–3 kyr [from MIS 5 (237 ppmv on average) to MIS 3 (209 ppmv on average)]. The average decrease rate is found to be about -14 ppmv/kyr comparable to the Byrd study (-11 ppmv/kyr) (6). In addition, a rapid drop of about 10 ppmv within 350 y is found at the beginning of this transition comparable in duration and magnitude to a rapid increase found during the last deglaciation (21). Various processes are candidates to explain changes of CO_2, such as the remarkable CO_2 decrease during the MIS 5–4 transition, or the millennial-scale variations associated with the CDM (6, 22). In the following, we discuss mechanisms that could potentially explain the increase of the lag of CDM relative to the DO event from MIS 5 to 3 as identified in our CO_2 records and, hence, focus on the CO_2 increase after the DO events which explains–in case of the MIS 3 CDM–about one-third of the total CDM amplitude.

Discussion

Proxy data suggest that DO events had a significant impact on terrestrial vegetation in the northern hemisphere and, therefore, changes in the terrestrial carbon storage may have contributed to the CDM recorded in the ice cores. Around a western European latitudinal transect, forests grew in the course of DO events and shrank when Greenland was in the cold phase (23). Since terrestrial vegetation has a reaction time to abrupt climate changes of about 250 y (15), and large forest growth is thought to cause a net uptake of CO_2 from the atmosphere, such an uptake cannot explain a prolonged carbon release to the atmosphere as evidenced in the observed lag of the CDM relative to DO onsets during MIS 3. Furthermore, during MIS 5, the European transect was covered with more forest than later in the glacial (23) counteracting the decrease of CO_2 at the MIS 5–4 transition. Since the warming of DO events spreads at least from the North Atlantic to eastern China (16), a large part of the terrestrial biosphere probably took up CO_2 from the atmosphere in the course of the DO events, which is also suggested from model experiments (17,18,24). Hence, a change in the terrestrial biosphere carbon storage is unlikely to be responsible for the lag of CDM, although regional differences of the terrestrial vegetation are clearly too complex to scale the biosphere behavior to the whole globe. The response of the soil carbon to rapid warmings is even more

uncertain but model experiments suggest that soil carbon changes contribute only little to the atmospheric CO_2 concentration during DO-like events (18).

Dust input in the Southern Ocean [approximated by the non-sea salt (nss) Ca^{2+} flux in the EDML ice core] (Fig. 1) (19) also provides iron to the surface water which is considered a fertilizer for marine biology and, hence, can influence atmospheric CO_2. If changes in dust input caused the detected shift in the phase lag of CDM relative to the DO onset, the peaks of the dust input should also shift relative to AIM events from MIS 3 to 5. Here, we compare the phasing between $nssCa^{2+}$ as proxy for Fe input into the Southern Ocean, on the one hand, and water isotopes in the ice as Southern Ocean temperature indicator, on the other hand. Due to the large error in the gas age/ice age difference, a direct comparison of CO_2 and $nssCa^{2+}$ is not conclusive. Neither a clear shift of dust input relative to AIM events between MIS 3 and 5, nor a significant dust decrease after the peak of AIM events, is recorded. Furthermore, latest carbon cycle model experiments show that dust flux variations associated with a full AIM event (changes of factor 10) explain only a 4–8 ppmv CO_2 change (25). Accordingly, the dust fertilization effect has most likely contributed to the CO_2 increase before the onset of DO events but is an unlikely explanation for the shift in the phasing between CDM and DO events.

Changes in ocean circulation and the distribution of major water masses can influence atmospheric CO_2 concentrations (22, 26). One proxy for ocean hydrographic changes is the Nd isotope ratio in ocean sediment cores (expressed as ε_{Nd}), which traces deep water origin at the drill site (Fig. 3C) (27). An Indian Ocean record (28) shows stable ε_{Nd} values at Holocene values (about −8.8) during the whole MIS 5, indicating continuous presence of North Atlantic Deep Water (NADW) at that site. At the transition into MIS 4, there is a pronounced increase in ε_{Nd} to glacial values (about −7.1) within a few thousand years indicating a decrease of NADW reaching this site. In a higher resolved record of the southern Atlantic (29), a similar change is found at the MIS 5-4 transition from about −8.3 (late MIS 5) to −7.3 (MIS 4). At that site, the late MIS 5 level seems to be slightly higher than the Holocene level (−8.9). Furthermore, a slowdown of the AMOC at the MIS 5–4 transition, with relatively constant NADW export during MIS 5, has been reported from a sediment core in the deep northeastern Atlantic (Fig. 3F) (30). Taken together, these records indicate that at the MIS 5–4 transition deep ocean circulation in the Atlantic changed significantly from a modern-like situation, where NADW flows southward at depth to the southern Atlantic and then partly into the Indian Ocean, to a glacial situation with a slower AMOC and a shallower Glacial North Atlantic Intermediate Water (GNAIW) cell lying on top of an increased Antarctic Bottom Water (AABW) mass extending into the North Atlantic (Fig. 4) (26). The salient difference from MIS 5 to MIS 3 conditions therefore appears to be the presence of a weakly ventilated, carbon-rich water mass in the deep Atlantic Ocean. This is supported by a synthesis of benthic $\delta^{13}C$ records (31), which shows a decrease of $\delta^{13}C$ in the Atlantic basin and the Southern Ocean at the MIS 5–4 transition (Fig. 3E). This indicates an increase in respired carbon in these bottom waters and could be partly responsible for the atmospheric CO_2 decrease at the MIS 5–4 transition.

During the AIM events 8, 12, 14, and likely also 17, the southern Atlantic ε_{Nd} record–and somewhat also weaker in the Indian ocean record–suggests associated variations of NADW reaching these sites (Fig. 3C) (28, 29). In the case of the southern Atlantic record, synchronous $\delta^{13}C$ variations have been found, indicating the possibility of circulation-driven changes in the carbon content of deep waters during these variations (29). Moreover, increased upwelling in the Southern Ocean of deep ocean waters has been inferred from records of opal accumulation associated with AIM events 8, 12, 14, 17, 19, 20, and possibly 21
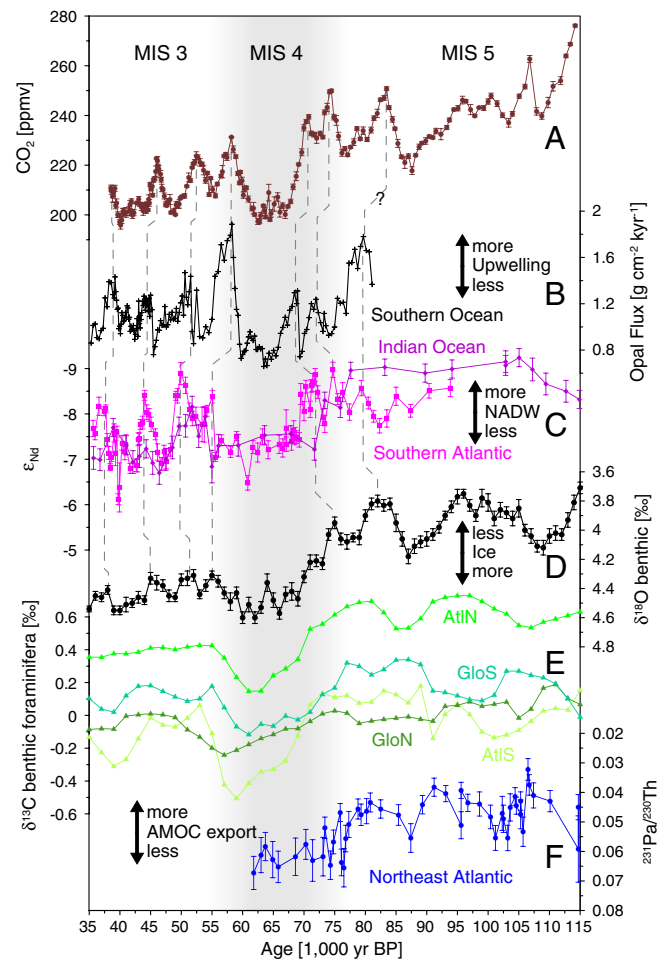
Fig. 3. Compilation of atmospheric CO_2 and ocean sediment records from 115 to 35 kyr BP. (A) CO_2 composite record from TALDICE and EDML ice core. (B) Opal Flux record from a sediment core at the polar front region in the Southern Ocean (32). Changes in these data are interpreted as changes in marine productivity in the polar front region. (C) Nd-isotope record from two sediment cores from the Indian (3 °N, 76 °E, 3,800 m below sea level [b.s.l.]) and Southern Atlantic ocean (40 °S, 8 °E, 4,981 m b.s.l.) indicating which portion of the local water masses originated from NADW (28, 29). (D) Benthic foraminifera $\delta^{18}O$ composite as a combined proxy of total ice volume/sea level and deep ocean temperature (41). (E) $\delta^{13}C$ data of benthic foraminifera from sediment cores below 2,500 m depth in the ocean. The four lines represent averages of the corresponding data from (31) over the following four different sectors: Atlantic North (AtlN) contains the data from the Atlantic basin between 90 °N and 40 °S and Atlantic South (AtlS) those between 40 °S to 90 °S. Global North (GloN) and Global South (GloS) include all data from (31) of the same latitudinal sectors as before (GloS: 40 S–90 °S; GloN: 90 °N–40 °S) except those from the Atlantic. $\delta^{13}C$ values of benthic foraminifera are partly linked to the respired carbon content of the local deep ocean waters, hence, age of the water mass. (F) $^{231}Pa/^{230}Th$ record from a sediment core in the northeastern Atlantic (30) (39 °N, 13 °W, 3,547 m b.s.l.) interpreted as proxy of AMOC export strength. The gray-shaded area indicates MIS 4. The dashed lines indicate likely relations between CDM and variations in the sediment records. All records are plotted on their own age scales.

(Fig. 3B) (32). These millennial–scale variations in the sediment proxies and the differences in ocean hydrography between MIS 5 and 3 could explain the different characteristics of CDM between MIS 3 and 5 in the following way: Before the DO onset of a MIS 3 type event, the Atlantic ocean is in a glacial state with a carbon-rich and expanded AABW and a shallower GNAIW cell (Fig. 4). At the DO onset, the AMOC accelerates rapidly bringing heat to the north but also causes–at least during major events–a resumption of NADW formation. This leads to increased ventilation of
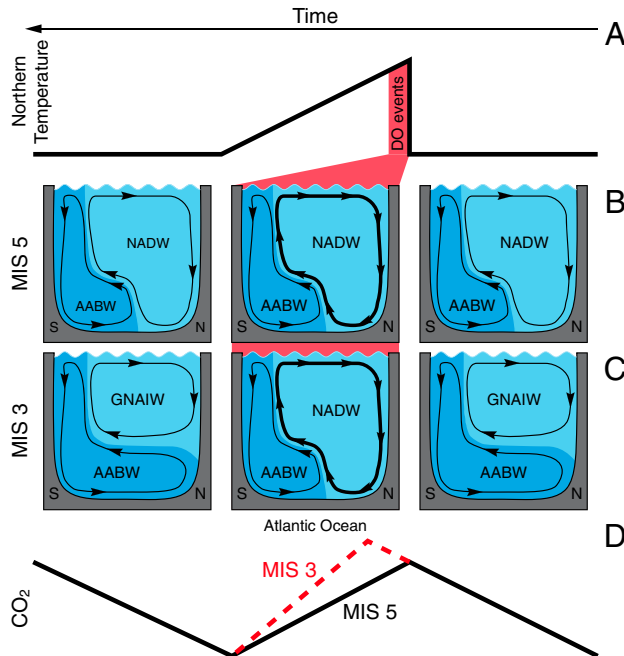
Fig. 4. Illustration of suggested water mass changes during DO events. (*A*) Schematic evolution of Greenland temperature during a DO event. (*B*) Schematic time slices of North Atlantic deep water mass (NADW, light blue) and Antarctic bottom water mass distributions (AABW, dark blue) as well as circulation (arrows) states in the Atlantic Ocean during MIS 5 type DO events. (*C*) Same as in (*B*) but with presence of Glacial North Atlantic Intermediate Water mass (GNAIW, light blue) as suggested for MIS 3 type DO events. (*D*) Idealized evolution of atmospheric CO_2 during a MIS 5 (black line) and MIS 3 type DO event (black plus red dashed line).

the deep Atlantic Ocean associated with an expansion of the NADW cell at depth at the expense of AABW and an upwelling of carbon-rich waters in the south. The ventilation of carbon-rich waters adds CO_2 to the atmosphere for another 500 to 1,000 y while NADW formation continues until the CO_2 release is counterbalanced by decreasing southern temperatures and a re-expansion of the AABW mass and the associated carbon pool in the deep ocean. The crucial difference of the MIS 5 events compared to the MIS 3 events is the modern-like ocean state on which DO events are superimposed (Fig. 4). During MIS 5, AMOC also accelerates at the DO onset. However, we conclude that this acceleration releases significantly less CO_2 to the atmosphere than during MIS 3, since the additional carbon-enriched AABW reservoir was not as far extended into the North Atlantic as during MIS 3.

For the MIS 3 events, the TALDICE records show that atmospheric CO_2 increases after the DO event for another 8.4 ± 2.6 ppmv equivalent to 18 ± 5.5 GtC (Fig. 2, *Insets*). According to our hypothesis, this carbon should be provided by exchanging the deep waters in the North Atlantic from carbon enriched AABW to NADW. Is there enough carbon stored in AABW in the North Atlantic during MIS 3 stadial conditions? Multi-box modeling of the glacial carbon cycle (33) found a dissolved inorganic carbon (DIC) content of glacial AABW of nearly 2,600 μmol/kg whereas glacial North Atlantic waters contain about 2100 μmol/kg. Thus, leaving everything else unchanged, replacing this AABW by NADW changes the DIC content in the deep North Atlantic by about 500 μmol/kg. This replacement starts at the onset of the DO event. Using an exchanged water volume of 5.5×10^{16} m^3 in the North Atlantic from 0° to 60 °N, 60° longitude, and from 3,500 to 5,000 m water depth, 330 GtC could be released to the atmosphere by this exchange. However, the largest amount of that CO_2 is taken up by the surface ocean and is mixed again into the global ocean. The proportion of CO_2 that could remain in the atmosphere after such a release is given by

the ratio of the undisturbed atmospheric carbon pool and the ocean carbon pool corrected for the buffer factor (approximately 11). This results in a net input from the ocean into the atmosphere of 36 GtC, i.e., about twice as much as needed to explain the CDM lag.

Clearly, this represents a rough estimate that is only intended to show that in principle enough carbon is available in the extended AABW to explain the CDM lag. The temporal constraints recorded in the different proxies are not strong enough to argue for or against this mechanism, because a common time scale for the various paleorecords in Fig. 3 is missing. Furthermore, the estimates of the size of the carbon reservoirs–in particular the DIC content of AABW and NADW during glacial times–is uncertain and model dependent, although even a two times smaller DIC change could still account for the observed CO_2 change. The assumption that all ventilated waters reach the surface and release CO_2 provides an upper limit. Finally, our estimate only accounts for the overall amplitude of the CO_2 change, but it cannot constrain the temporal dynamics of these changes. Accordingly, we cannot make a quantitative statement on the size of the phase lag between the CO_2 maximum and the onset of the DO events based on this calculation.

Support for our hypothesis could come from an analysis of carbon isotopes at atmospheric CO_2 (^{13}C) during CDM. So far, only one study presents data over CDM 12 from two different ice cores (34). The record from the Berkner Island ice core indicates a decrease in $\delta^{13}CO_2$ in the atmosphere at the peak of CDM 12 in line with a release of ^{13}C depleted carbon from the deep ocean; however, the data uncertainty is still large. Better constraints for the CDM patterns can be provided by improved reconstructions of $\delta^{13}CO_2$ signals during several CDM and a common age scale of the different climate archives (35).

Coupled carbon cycle-climate model simulations may provide further quantitative insight. The classical approach to model abrupt climate changes associated with DO events was to trigger a change in the AMOC by perturbing the surface freshwater balance in the Atlantic. On the one hand, such experiments show atmospheric CO_2 variations, which are consistent in amplitude with the CDM found in the ice cores (17,18,24, 36–38). On the other hand, the different model studies are inconsistent with respect to the major carbon reservoir changes responsible for the atmospheric CO_2 variations. Under preindustrial conditions, most models respond with a release of CO_2 from the terrestrial biosphere and an uptake of CO_2 by the ocean to a reduction of the AMOC (17,18,24), however, also an opposite response is found in one study (38). Under glacial conditions, the models show a larger contribution of changes in the ocean inventory compared to those in other reservoirs (24, 37, 38). One model (24) even shows decreasing atmospheric CO_2 concentrations during the cold phase in Greenland when the AMOC is reduced, which is inconsistent with the available CO_2 records. From the available model studies, only one exhibited a lag of the CDM with respect to the AMOC resumption (38). In those simulations, the source of the carbon after the AMOC resumption seems to be the ocean, however, whether it originates from the mechanism as described here is not clear. Taken together, models still do not provide a consistent picture regarding the causes of CO_2 variations associated with millennial scale climate variations. Hence, a quantitative investigation of our hypothesis with current coupled carbon cycle-climate models is not yet feasible. Nevertheless, further model studies of the coupled carbon cycle-climate system during the last ice age will be indispensable to understand the subtle, and yet significant, mode changes discovered here.

Materials and Methods

The basic measurement technique is analogous to ref. 39. Here, modifications made in this study are discussed. Due to gas fractionation which occurs in the Bubble-Clathrate Transformation Zone (BCTZ) and which persists also just below the BCTZ (7), six to 10 replicate measurements at the TALDICE core

between 35 and 42 kyr BP have been performed to reduce the measurement uncertainties (usually four replicates). Since the fractionation is strongest just below the BCTZ (at 35 kyr BP in the TALDICE core on our time scale) and decreases with distance from the BCTZ due to diffusion in the ice, we could not reduce the uncertainty sufficiently in the TALDICE record between 35 kyr and 38 kyr with this approach (Fig. 1, pink area). This also applies to the EDML record between 30 kyr and 45 kyr BP (7). Nevertheless, the uncertainty between the time span from 38 to 42 kyr BP in the TALDICE record could be reduced to 1.5 ppmv (one sigma), which is comparable to 1.3 ppmv in the EDML record (Fig. 1). From 42 kyr BP back to the end of the TALDICE record, the average uncertainty is just 1.0 ppmv, owing to the good ice quality and the high air content (about 10% higher than the EDML ice core) of the TALDICE core. Furthermore, the TALDICE core has a higher accumulation rate than central east Antarctic ice cores, providing a narrower age distribution of the air bubbles occluded and thus making it a very suitable core for studying the atmospheric variability during MIS 3.

1. North Greenland Ice Core Project Members (2004) High-resolution record of Northern Hemisphere climate extending into the last interglacial period. *Nature* 231:147–151.
2. Huber C, et al. (2006) Isotope calibrated Greenland temperature record over Marine Isotope Stage 3 and its relation to CH_4. *Earth Planet Sci Lett* 243:504–519.
3. EPICA Community Members (2006) One-to-one coupling of glacial climate variability in Greenland and Antarctica. *Nature* 444:195–198.
4. Stocker TF, Johnson J (2003) A minimum thermodynamic model for the bipolar seesaw. *Paleoceanography* 18 art. no. 1087.
5. Indermühle A, Monnin E, Stauffer B, Stocker TF, Wahlen M (2000) Atmospheric CO_2 concentration from 60 to 20 kyr BP from the Taylor Dome ice core, Antarctica. *Geophys Res Lett* 27:735–738.
6. Ahn J, Brook EJ (2008) Atmospheric CO_2 and climate on millennial time scales during the last glacial period. *Science* 322:83–85.
7. Lüthi D, et al. (2010) CO_2 and O_2/N_2 variations in and just below the bubble-clathrate transformation zone of Antarctic ice cores. *Earth Planet Sci Lett* 297:226–233.
8. Schüpbach S, Federer U, Bigler M, Fischer H, Stocker TF (2011) A refined TALDICE-1a age scale from 55 to 112 ka before present for the Talos Dome ice core based on high-resolution methane measurements. *Climate of the Past* 7:1–16.
9. Buiron D, et al. (2011) TALDICE-1 age scale of the Talos Dome deep ice core, East Antarctica. *Climate of the Past* 7:1–16.
10. Schilt A, et al. (2010) Atmospheric nitrous oxide during the last 140,000 years. *Earth Planet Sci Lett* 300:33–43.
11. Capron E, et al. (2010) Synchronizing EDML and NorthGRIP ice core using $\delta^{18}O$ of atmospheric oxigen ($\delta^{18}O_{atm}$) and CH_4 measurements over MIS5 (80–123 kyr). *Quaternary Science Reviews* 29:222–234.
12. Petit JR, et al. (1999) Climate and atmospheric history of the past 420,000 years from the Vostok ice core, Antarctica. *Nature* 399:429–436.
13. Loulergue L, et al. (2007) New constraints on the gas age-ice age difference along the EPICA ice cores, 0–50 kyr. *Climate of the Past* 3:527–540.
14. Bereiter B, Schwander J, Lüthi D, Stocker TF (2009) Change in CO_2 concentration and O_2/N_2 ratio in ice cores due to molecular diffusion. *Geophys Res Lett* 36:1–5, AGU identifier: L05703 doi: 10.1029/2008GL036737.
15. Scholze M, Knorr W, Heimann M (2003) Modeling terrestrial vegetation dynamics and carbon cycling for an abrupt climatic change event. *Holocene* 13:327–333.
16. Wang YJ, et al. (2001) A high-resolution absolute-dated late Pleistocene monsoon record from Hulu Cave, China. *Science* 294:2345–2348.
17. Obata A (2007) Climate-carbon cycle model response to freshwater discharge into the North Atlantic. *J Clim* 20:5962–5976.
18. Bozbiyik A, Steinacher M, Joos F, Stocker TF, Menviel L (2011) Fingerprints of changes in the terrestrial carbon cycle in response to large reorganizations in ocean circulation. *Climate of the Past* 7:319–338.
19. Fischer H, et al. (2007) Reconstruction of millennial changes in dust emission, transport and regional sea ice coverage using the deep EPICA ice cores from the Atlantic and Indian Ocean sector of Antarctica. *Earth Planet Sci Lett* 260:340–354.
20. Schneider R (2011) Quantifying past changes of the global carbon cycle based on $\delta^{13}CO_2$ measurements in Antarctic ice cores. PhD thesis (Univ of Bern).
21. Monnin E, et al. (2001) Atmospheric CO_2 concentrations over the last glacial termination. *Science* 291:112–114.
22. Fischer H, et al. (2010) The role of Southern Ocean processes in orbital and millennial CO_2 variations—A synthesis. *Quat Sci Rev* 29:193–205.
23. Sanchez Goni MF, et al. (2008) Contrasting impacts of Dansgaard-Oeschger events over a western European latitudinal transect modulated by orbital parameters. *Quat Sci Rev* 27:1136–1151.
24. Menviel L, Timmermann A, Mouchet A, Timm O (2008) Meridional reorganizations of marine and terrestrial productivity during Heinrich events. *Paleoceanography* 23:1–19, AGU identifier: PA1203 doi: 10.1029/2007PA001445.
25. Parekh P, Joos F, Müller SA (2008) A modeling assessment of the interplay between aeolian iron fluxes and iron-binding ligands in controlling carbon dioxide fluctuations during Antarctic warm events. *Paleoceanography* 23:1–14, AGU identifier: PA4202 doi:10.1029/2007PA001531.
26. Sigman DM, Hain MP, Haug GH (2010) The polar ocean and glacial cycles in atmospheric CO_2 concentration. *Nature* 466:47–55.
27. Rempfer J, Stocker TF, Joos F, Dutay J, Siddall M (2011) Modeling Nd-isotopes with a coarse resolution ocean circulation model: Sensitivities to model parameters and source/sink distributions. *Geochim Cosmochim Acta* 75:5927–5950.
28. Piotrowski AM, et al. (2009) Indian Ocean circulation and productivity during the last glacial cycle. *Earth Planet Sci Lett* 285:179–189.
29. Piotrowski AM, Goldstein SL, Hemming SR, Fairbanks RG (2005) Temporal relationships of carbon cycling and ocean circulation at glacial boundaries. *Science* 307:1933–1938.
30. Guihou A, et al. (2010) Late slowdown of the Atlantic Meridional Overturning Circulation during the last glacial inception: New constraints from sedimentary ($^{231}Pa/^{230}Th$). *Earth Planet Sci Lett* 289:520–529.
31. Oliver KIC, et al. (2010) A synthesis of marine sediment core $\delta^{13}C$ data over the last 150,000 years. *Clim Past* 6:645–673.
32. Anderson RF, et al. (2009) Wind-driven upwelling in the Southern Ocean and the deglacial rise in atmospheric CO_2. *Science* 323:1443–1448.
33. Köhler P, Fischer H, Munhoven G, Zeebe RE (2005) Quantitative interpretation of atmospheric carbon records over the last glacial termination. *Global Biogeochem Cycles* 19:1–24, AGU identifier: GB4020 doi: 10.1029/2004GB002345.
34. Schaefer H, et al. (2011) On the suitability of partially clathrated ice for analysis of concentration and $\delta^{13}C$ of palaeo-atmospheric CO_2. *Earth Planet Sci Lett* 307:334–340.
35. Leduc G, Thouveny N, Bourlès DL, Blanchet CL, Carcaillet JT (2006) Authigenic $^{10}Be/^9Be$ signature of the Laschamp excursion: A tool for global synchronization of paleoclimatic archives. *Earth Planet Sci Lett* 245:19–28.
36. Marchal O, Stocker TF, Joos F (1998) Impact of oceanic reorganizations on the ocean carbon cycle and atmospheric carbon dioxide content. *Paleoceanography* 13:225–244.
37. Schmittner A, Galbraith ED (2008) Glacial greenhouse-gas fluctuations controlled by ocean circulation changes. *Nature* 456:373–376.
38. Bouttes N, Roche DM, Paillard D (2011) Systematic study of the fresh water fluxes impact on the carbon cycle. *Clim Past* 7:1363–1392.
39. Lüthi D, et al. (2008) High-resolution carbon dioxide concentration record 650,000–800,000 years before present. *Nature* 453:379–382.
40. Stenni B, et al. (2010) The deuterium excess records of EPICA Dome C and Dronning Maud Land ice cores (East Antarctica). *Quat Sci Rev* 29:146–159.
41. Lisiecki LE, Raymo ME (2005) A Pliocene-Pleistocene stack of 57 globally distributed benthic $\delta^{18}O$ records. *Paleoceanography* 20:1–17, AGU identifier: PA1003 doi:10.1029/2004PA001071.